CHEMISTRY OF MATERIALS

Article

pubs.acs.org/cm

Structural Evolution of Ag−Pd Bimetallic Nanoparticles through Controlled Galvanic Replacement: Effects of Mild Reducing Agents

Hao Jing and Hui Wang*

Department of Chemistry and Biochemistry, University of South Carolina, Columbia, South Carolina 29208, United States

Supporting Information

ABSTRACT: Galvanic replacement provides a simple but versatile way of converting less noble metallic solid nanoparticles into structurally more complex multimetallic hollow nanostructures composed of more noble metals. In contrast to the well-studied Ag−Au bimetallic hollow nanostructures, limited success has been achieved on the geometry control over Ag−Pd bimetallic nanoparticles through galvanic replacement reactions. Here we demonstrate that the capability of geometry control over Ag−Pd bimetallic hollow nanostructures through nanoscale galvanic replacement can be greatly enhanced by the use of appropriate mild reducing agents, such as ascorbic acid and formaldehyde. With the aid of mild reducing agents, we have been able to fine-tailor the compositions, interior architectures, and surface morphologies of Ag−Pd bimetallic hollow nanoparticles with increased structural complexity through surface ligand-free galvanic replacement processes at room temperature. This reducing agent-mediated galvanic replacement provides a unique way of achieving both enhanced optical tunability and optimized catalytic activities through deliberate control over the geometries of complex Ag−Pd bimetallic nanoparticles.

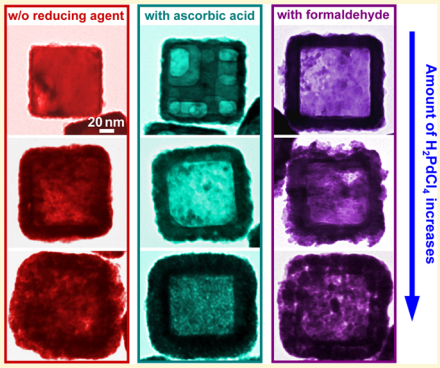

INTRODUCTION

Nanoscale galvanic replacement provides a versatile and elegant approach to the transformation of monometallic solid nanoparticles into more complex multimetallic nanostructures with hollow interiors.[1−4] Over the past decade, remarkable progress has been made on the use of galvanic replacement for generating complex multimetallic hollow nanostructures, Ag−Au bimetallic hollow nanoparticles in particular, with tunable and well-controlled properties. Ag nanoparticles with well-defined shapes, such as nanospheres, nanocubes, and nanoprisms, are commonly used as the sacrificial templates that evolve into Ag−Au bimetallic nanoshells, nanoboxes, nanocages, and nanoframes upon galvanic replacement with $AuCl_4^-$ under appropriate conditions.[2,3,5−8] While the starting templates define the overall shapes of the resulting hollow nanostructures, the wall thickness, compositions, crystallinity, and porosity are all controlled essentially by the interfacial alloying and dealloying processes associated with the galvanic replacements.[2,3,9,10] Via the coupling of galvanic replacement with sequentially deposited templates,[11−14] the Kirkendall effects,[4] or combined co-reduction and corrosion,[15−17] it becomes possible to controllably create a variety of nanostructures with increasingly sophisticated interior and surface architectures, such as yolk−shell nanorattles,[11−13] multilayered nanoshells,[11] multichambered nanoboxes,[4] and three-dimensional ultrathin nanoframes.[16,17] The Ag−Au bimetallic hollow nanoparticles forming through such galvanic replacements exhibit plasmon-dominated optical properties that are highly tunable in the visible and near-infrared spectral regions, endowing these nanoparticles with great promise for photonic and biomedical applications.[7,18−21]

Similarly, Ag−Pd and Ag−Pt bimetallic hollow nanostructures can also be fabricated through galvanic replacements when the metal salt precursor is switched from $AuCl_4^-$ to $PdCl_4^-$ and $PtCl_4^-$, respectively.[22−27] Pd- or Pt-containing alloy or heterostructured nanoparticles with hollow interiors and open surface structures, such as porous nanocages and nanoframes, are of particular interest for high-performance nanocatalysis because of their high surface-to-volume ratio, excellent surface accessibility, nanocage confinement effects, and optimal use of the catalytically active precious metals.[27−31] However, direct galvanic replacement offers rather poor control over the geometries of Ag−Pd and Ag−Pt bimetallic hollow nanostructures in contrast to their Ag−Au counterparts, thereby limiting the tunability of the optical and catalytic properties of the particles.[2,3,22] Because of the poor miscibility between Ag and Pt, the Ag−Pt hollow nanostructures obtained through galvanic replacement typically exhibit ill-defined overall morphologies with bumpy and polycrystalline heterostructured walls.[22,32] In contrast, Ag−Pd bimetallic nanoboxes enclosed by smooth, continuous Ag−Pd alloy walls can be obtained through galvanic replacement primarily because Ag has higher miscibility with Pd than with Pt.[2,22,33] However, the synthesis of Ag−Pd hollow nanoparticles with open structures, for example, nanocages or nanoframes, has been challenging

Received: January 16, 2015
Revised: February 10, 2015
Published: February 26, 2015

DOI: 10.1021/acs.chemmater.5b00199
Chem. Mater. 2015, 27, 2172−2180

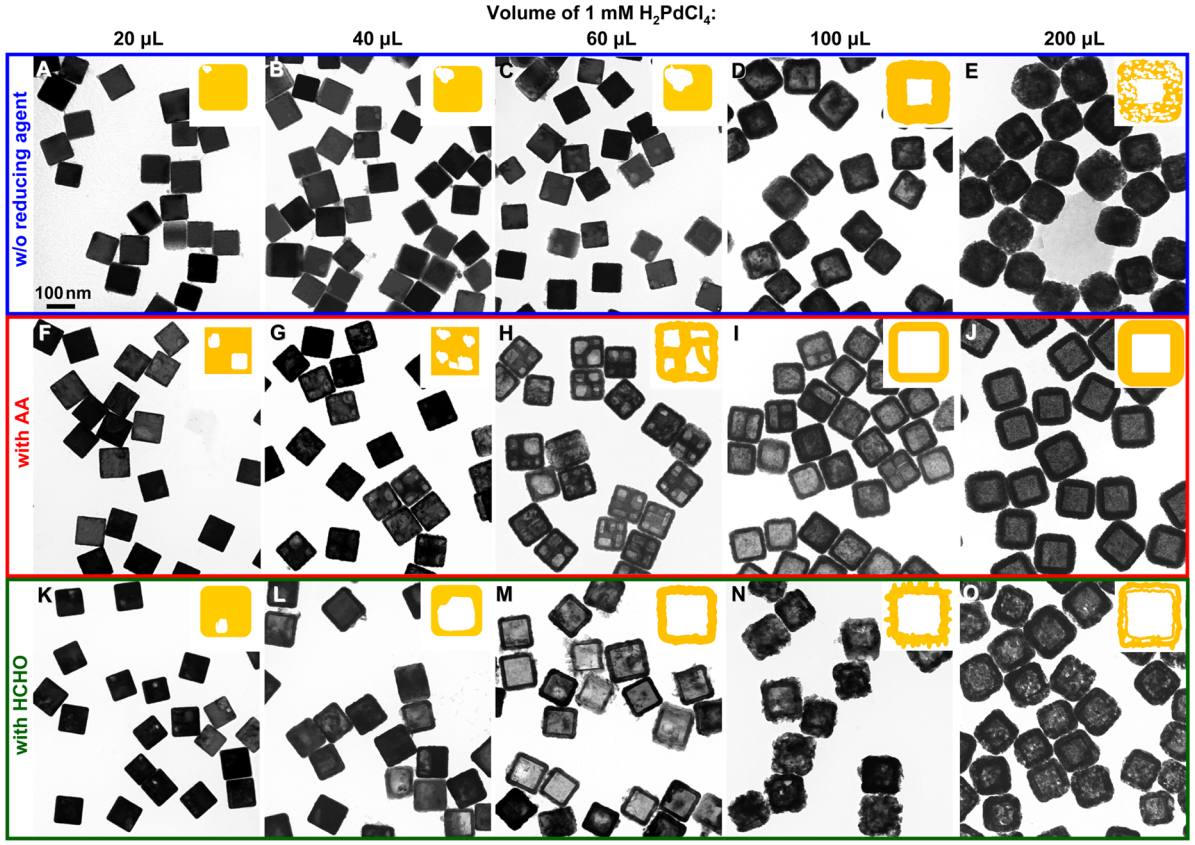

Figure 1. TEM images of Ag−Pd bimetallic hollow nanostructures synthesized through galvanic replacement of Ag nanocubes with H_2PdCl_4 under various conditions: (A) 20 μL of 1 mM H_2PdCl_4, without reducing agents; (B) 40 μL of 1 mM H_2PdCl_4, without reducing agents; (C) 60 μL of 1 mM H_2PdCl_4, without reducing agents; (D) 100 μL of 1 mM H_2PdCl_4, without reducing agents; (E) 200 μL of 1 mM H_2PdCl_4, without reducing agents; (F) 20 μL of 1 mM H_2PdCl_4, with AA; (G) 40 μL of 1 mM H_2PdCl_4, with AA; (H) 60 μL of 1 mM H_2PdCl_4, with AA; (I) 100 μL of 1 mM H_2PdCl_4, with AA; (J) 200 μL of 1 mM H_2PdCl_4, with AA; (K) 20 μL of 1 mM H_2PdCl_4, with HCHO; (L) 40 μL of 1 mM H_2PdCl_4, with HCHO; (M) 60 μL of 1 mM H_2PdCl_4, with HCHO; (N) 100 μL of 1 mM H_2PdCl_4, with HCHO; and (O) 200 μL of 1 mM H_2PdCl_4, with HCHO. All the TEM images share the same scale bar in panel A. The particle morphologies are schematically illustrated as an inset in the top right corner of each image. The cartoons illustrate only the structures of the nanoparticles without showing the compositional distributions of the particles.

because $PdCl_4^-$ is unable to dealloy and consequently introduce nanoporosity into the Ag−Pd alloy nanobox walls that form at the earlier stage of the galvanic replacement reaction.[2,22,34]

Here we show that mild reducing agents, such as ascorbic acid (AA) and formaldehyde (HCHO), fine-regulate the alloying and dealloying processes involved in the galvanic replacement between Ag nanocubes and H_2PdCl_4 without the help of any surface-capping ligands at room temperature. This reducing agent-mediated galvanic replacement allows us to fine-tailor the geometries of the Ag−Pd bimetallic hollow nanostructures with increased architectural complexity and thus greatly enhances our capabilities to both fine-tune the optical characteristics and optimize the catalytic performance of Ag−Pd bimetallic nanostructures.

RESULTS AND DISCUSSION

While the galvanic replacement of Ag nanoparticles with $AuCl_4^-$ is spontaneous and kinetically fast at room temperature, exposing Ag nanoparticles to Na_2PdCl_4 at room temperature does not result in any observable galvanic replacement over extended time periods because the standard electrode potential of $PdCl_4^{2-}$/Pd (0.591 V vs SHE) is even lower than that of Ag^+/Ag (0.800 V vs SHE).[26] However, when the solution is heated to 100 °C, $PdCl_4^{2-}$ ions may be thermally decomposed to form Pd^{2+} with a standard reduction potential of Pd^{2+}/Pd (0.951 V vs SHE) more positive than that of Ag^+/Ag, making the galvanic replacement thermodynamically spontaneous.[22,25,26] Kinetically, increasing the reaction temperature favors the atomic interdiffusion between Ag and Pd during alloying and dealloying, which facilitates the interior hollowing process upon galvanic replacement. It has been reported that galvanic replacement of Ag nanocubes and nanoprisms with Na_2PdCl_4 at 100 °C results in the rapid formation of Ag−Pd alloy nanoboxes and triangular nanoframes, respectively.[22,26] Here we used H_2PdCl_4 as the Pd precursor and conducted the galvanic replacement reaction in an acidic environment (pH ∼3) at room temperature in the absence of any additional Cl^- anion-containing electrolytes or ligands. Under these conditions, the H_2PdCl_4 solution is composed of a series of Pd(II) species at equilibrium concentrations with a significant fraction of Pd(II) existing in the form of free Pd^{2+} ions,[35] which thermodynamically drive the galvanic replacement reaction.

We used single-crystalline Ag nanocubes with an average edge length of 100 nm (Figure S1 of the Supporting Information) as the sacrificial template for the galvanic replacement. The colloidal Ag nanocubes displayed four distinct peaks in the extinction spectrum, which were assigned, in order from longer to shorter wavelengths, to the dipole, quadrupole, octupole, and higher-order multipole plasmon resonances, respectively, according to previously reported

DOI: 10.1021/acs.chemmater.5b00199
Chem. Mater. 2015, 27, 2172−2180

finite-difference time domain (FDTD)[36] and discrete dipole approximation (DDA) calculations.[37] To study the galvanic replacement-induced structural evolution, we first titrated 30 μL of colloidal Ag nanocubes (5×10^{10} particles mL^{-1}) with H_2PdCl_4 in the absence of any reducing agents at room temperature. The pH values of the reaction mixtures were measured to be in the range of 2.6−3.2 upon the addition of various amounts of H_2PdCl_4. Panels A−E of Figure 1 show the transmission electron microscopy (TEM) images of the Ag−Pd bimetallic nanoparticles obtained upon completion of galvanic replacement with various amounts of H_2PdCl_4. When 20 μL of 1 mM H_2PdCl_4 was introduced, small pits formed at the locations close to the nanocube corners (Figure 1A). The atomic step edges present at the nanocube corners may provide the most reactive sites for the initiation of pitting.[22] At the same time, Pd nanocrystallites (3−6 nm in size) were deposited on the outer surfaces of the nanocubes as a consequence of galvanic replacement. The initiation of pitting and the concurrent surface deposition of Pd were more clearly visualized in the TEM image with a higher magnification (Figure S2A of the Supporting Information). In the high-resolution TEM (HRTEM) image shown in Figure S2B of the Supporting Information, the lattice fringes corresponding to the (111) lattice of face-centered cubic Pd and the (200) lattice of face-centered cubic Ag were both clearly resolved, further verifying the deposition of Pd nanocrystals on the Ag surfaces. The deposited Pd nanocrysals showed different crystalline orientations with respect to the Ag nanocube core, indicating nonepitaxial Pd deposition on Ag upon initiation of galvanic replacement. Such nonepitaxial deposition may be the consequence of lattice mismatch between Ag and Pd, which could be further verified by the Moiré patterns in the HRTEM image. As the amount of H_2PdCl_4 increased, the size of cavities inside the nanocubes became larger and the edge length of the nanocubes increased slightly as more Ag was oxidized and more Pd was deposited on the nanocube surfaces (Figure 1B,C). Pd and Ag both have the same face-centered cubic structure and can interdiffuse to form alloys at room temperature.[33] Upon the introduction of 100 μL of 1 mM H_2PdCl_4, Ag−Pd bimetallic nanoboxes with smooth and continuous single-layer walls were obtained (Figure 1D). In comparison to the starting Ag nanocubes, a significant, ∼70% volume expansion was observed on the nanoboxes due to the Kirkendall effects[38] (Ag diffused faster than Pd during the alloying process). As previously reported by Xia and co-workers, Ag−Pd alloy nanoboxes could also be fabricated by reacting Ag nanocubes with Na_2PdCl_4 at 100 °C.[22] In contrast to the Ag−Au alloy nanoboxes that evolve into porous nanocages and eventually into nanofragments upon introduction of additional $HAuCl_4$, Ag−Pd alloy nanoboxes were found to be more stable and did not undergo any further structural changes in the presence of excessive Na_2PdCl_4 even at 100 °C.[2,22,34] It requires higher potentials to remove Ag from the Ag−Pd or Ag−Au alloys than from monometallic Ag because Ag can be stabilized when alloyed into a Au or Pd matrix. Given the small difference between the Pd and Ag reduction potentials, Na_2PdCl_4 lacks the capability to further dealloy Ag from the Pd−Ag alloy walls of the nanoboxes, thereby inhibiting the formation of porous Ag−Pd nanocages.[22,34] Interestingly, we found that when the volume of 1 mM H_2PdCl_4 further increased to 200 μL, the walls of the Ag−Pd nanoboxes became significantly thicker and much less dense with a large number of hierarchical nanoscale pores (Figure 1E). The porous nature of the nanobox walls was more clearly visualized by scanning electron microscopy (SEM) as shown in Figure S3 of the Supporting Information. This structural evolution can be interpreted mostly likely as the consequence of dealloying-driven reshaping of the Ag−Pd alloy walls, which became possible under our experimental conditions (acidic environment, room temperature). These porous Ag−Pd alloy nanoparticles were observed to be highly stable with no further morphological changes upon the introduction of additional H_2PdCl_4.

Introduction of a reducing agent to couple with the galvanic replacement allows one to manipulate the alloying and dealloying processes, which have a profound impact on the structural evolution of the nanoparticles. The use of AA as a mild reducing agent allowed the galvanic replacement reaction to proceed more rapidly, and a drastically different structural evolution process was observed on the Ag−Pd bimetallic nanoparticles (Figure 1F−J). The pH values of the reaction mixtures were essentially determined by H_2PdCl_4, as AA is a much weaker acid than H_2PdCl_4. No measurable change in pH was observed upon the addition of AA to the reaction mixtures. In the presence of AA, multiple interior cavities emerged in each nanocube upon galvanic replacement and gradually expanded as the amount of H_2PdCl_4 increased, resulting in the formation of multichambered nanoboxes (Figure 1G,H). SEM and higher-magnification TEM images (Figure S4A,B of the Supporting Information) showed that these multichambered nanoboxes were enclosed by relatively smooth, continuous outer walls. When 100 μL of 1 mM H_2PdCl_4 was introduced, the multiple nanochambers started to merge into one to form Ag−Pd bimetallic single-walled nanoboxes (Figure 1I). As the volume of 1 mM H_2PdCl_4 further increased to 200 μL, the nanobox walls became even thicker (Figure 1J). Although the outer surfaces of the nanoparticles appeared to be smooth in SEM images (Figure S4C of the Supporting Information), the higher-magnification TEM image (Figure S4D of the Supporting Information) clearly showed that the nanobox walls were essentially composed of small nanocrystals and were thus highly porous in nature. The thickness of the porous walls was determined by the amount of H_2PdCl_4 introduced. Increasing the amount of H_2PdCl_4 led to the formation of nanoparticles with thicker walls, while the size of the cubic interior cavity remained essentially unchanged, resulting in increased overall particle edge lengths (Figure S5 of the Supporting Information).

We also studied the structural evolution of the nanoparticles through galvanic replacement in the presence of another mild reducing agent, HCHO. The addition of HCHO did not result in any measurable changes in the pHs of the reaction mixtures. At relatively low Pd:Ag molar ratios (<100 μL of 1 mM H_2PdCl_4), only one cavity formed inside each nanocube upon galvanic replacement (Figure 1K−M). However, HCHO significantly promoted both the hollowing and alloying processes during the galvanic replacement, which is evident in the formation of larger interior cavities and more efficient Pd−Ag interdiffusion in comparison to those obtained in the absence of a reducing agent. With 60 μL of 1 mM H_2PdCl_4 added, Ag−Pd bimetallic single-walled nanoboxes with continuous walls were obtained (Figure 1M). The walls of these nanoboxes were significantly thinner than those obtained through the reducing agent-free galvanic replacement. Further increasing the amount of H_2PdCl_4 resulted in volume expansion, wall thickening, and surface roughening of the nanoboxes (Figure 1N). The nanoparticles eventually evolved

DOI: 10.1021/acs.chemmater.5b00199
Chem. Mater. 2015, 27, 2172−2180

into porous double-walled nanoboxes (Figure 1O and Figure S6 of the Supporting Information) when 200 μL of 1 mM H_2PdCl_4 was added. The porous double-walled nanoboxes were found to be structurally stable and did not undergo any further structural changes upon addition of excess H_2PdCl_4.

We used SEM and energy dispersive spectroscopy (EDS) to correlate the structures of individual nanoparticles with their compositions (Figure 2A–F). We used the Pd Lα and Ag Lβ lines in EDS spectra (see one example in Figure S7 of the Supporting Information) to quantify the Pd:Ag atomic ratios of the nanoparticles. In the absence of reducing agents, oxidative corrosion of Ag was initiated at locations close to the nanocube corners and Pd atoms were concurrently deposited onto the Ag surface (Figure 2A). The deposited Pd then migrated into Ag to form Ag–Pd alloy walls, while the interior hollow process proceeded. The increase in cavity size was accompanied by an increase in overall particle size as a consequence of the Kirkendall effect. The walls of the Ag–Pd alloy nanoboxes may undergo a dealloying-driven reshaping process upon introduction of additional H_2PdCl_4, leading to the formation of hollow nanoparticles with porous Ag–Pd alloy walls (Figure 2B). During the galvanic replacement, the Pd:Ag atomic ratios progressively increased with the amount of H_2PdCl_4 and reached a plateau upon the formation of the Ag–Pd alloy porous nanoboxes (Figure 2G). The compositional evolution (Figure 2G) correlated well with the changes in the particle sizes, with higher Pd:Ag atomic ratios corresponding to larger edge lengths (Figure 2H).

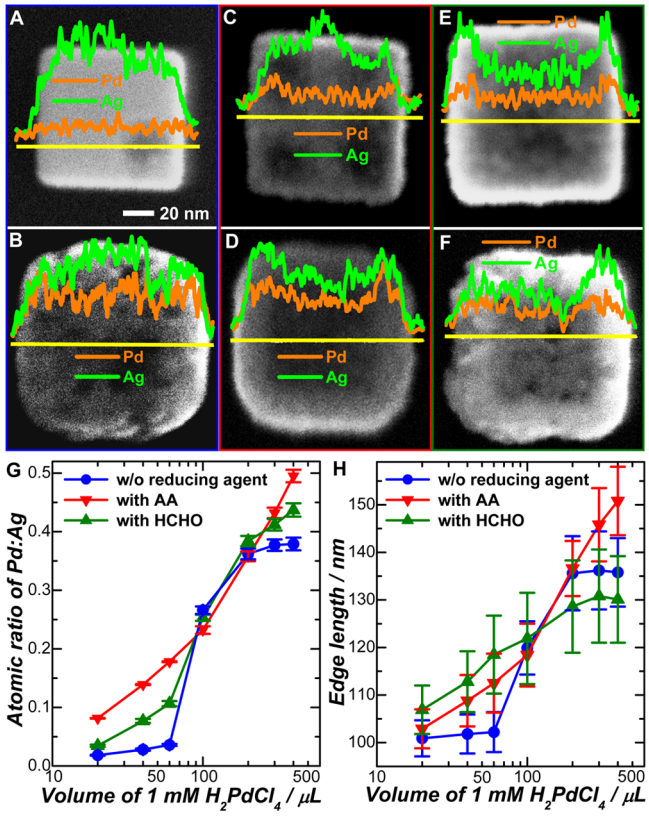

Figure 2. SEM images and EDS line scan elemental analysis of individual Ag–Pd bimetallic nanoparticles synthesized through galvanic replacement of Ag nanocubes with H_2PdCl_4 under various conditions: (A) 60 μL of 1 mM H_2PdCl_4, without reducing agents; (B) 200 μL of 1 mM H_2PdCl_4, without reducing agents; (C) 60 μL of 1 mM H_2PdCl_4, with AA; (D) 200 μL of 1 mM H_2PdCl_4, with AA; (E) 60 μL of 1 mM H_2PdCl_4, with HCHO; and (F) 200 μL of 1 mM H_2PdCl_4, with HCHO. All the SEM images share the same scale bar in panel A. (G) Evolution of Pd:Ag atomic ratios as the volume of 1 mM H_2PdCl_4 varies. The Pd:Ag atomic ratios were quantified by EDS measurements, and the error bars represent the standard deviations of EDS results on three samples synthesized under identical experimental conditions. (H) Evolution of the edge lengths of the nanoparticles as the volume of 1 mM H_2PdCl_4 solution varies. The error bars represent the standard deviations obtained from more than 200 nanoparticles in the TEM images for each sample.

In the presence of AA, the interior hollowing of the Ag templates was still driven by the galvanic replacement-induced oxidative corrosion of Ag, but the released Ag^+ ions were immediately reduced back to metallic Ag and were codeposited with Pd atoms onto the nanocube templates as Ag–Pd alloy layers. This was further verified by the electroless codeposition of Ag and Pd on Au nanoparticle surfaces in the presence of AA. We used quasi-spherical Au nanoparticles (Figure S8 of the Supporting Information) as the seeds to mediate the co-reduction of Ag and Pd by AA at room temperature. As shown in Figure S9 of the Supporting Information, with the Au seeds, AA was capable of reducing both Ag^+ and H_2PdCl_4 to form Au@Ag and Au@Pd core–shell nanoparticles, respectively. Interestingly, when Ag^+ and H_2PdCl_4 were added simultaneously into the reaction mixture, a thin shell of Ag–Pd alloy was deposited on the surface of each Au nanoparticle. It is worth mentioning that during galvanic replacement, the interior cavities of the Ag templates could also be accessed by Ag^+, H_2PdCl_4, and AA because of the presence of pinholes on the outer walls. Therefore, Ag–Pd alloy layers may also be deposited locally on the surfaces of the interior cavities, resulting in the formation of multiple cavities during galvanic replacement. The walls of the interior nanochambers were rich in Ag, while the outer walls of the particle were composed of the Ag–Pd alloy (Figure 2C). The co-reduction of Ag and Pd by AA facilitated the alloying process and consequently promoted galvanic replacement reactions. Therefore, the multichambered nanoboxes exhibited Pd:Ag ratios higher than those of the nanostructures obtained with the same amounts of H_2PdCl_4 but in the absence of reducing agents (Figure 2G). This is in striking contrast to the Ag–Au bimetallic nanoboxes whose Ag content was greatly enriched upon addition of AA to the galvanic replacement system.[15] At higher Pd:Ag molar ratios, the dealloying process started to dominate the structural evolution, which led to the conversion of thin smooth nanobox walls into thicker, porous walls with higher Pd:Ag ratios (Figure 2D). Both EDS (Figure 2D) and powder X-ray diffraction (PXRD) (Figure S10 of the Supporting Information) results verified that these single-walled hollow nanoparticles were composed of fully alloyed Ag–Pd. At this stage, AA was still able to facilitate the codeposition of Ag–Pd alloy onto the template surfaces, resulting in a continuous increase in wall thickness, overall particle size, and Pd:Ag atomic ratio as the amount of H_2PdCl_4 further increased (Figure 2G,H).

HCHO is a mild reducing agent whose reducing capability is even weaker than that of AA. As shown in Figure S11 of the Supporting Information, although HCHO was capable of reducing Pd(II) ions into metallic Pd onto the surfaces of Au nanoparticles to form Au@Pd core–shell nanoparticles, it was not strong enough to reduce Ag at room temperature. The Au nanoparticle-seeded reduction of coexisting Ag^+ and H_2PdCl_4 by HCHO at room temperature led to the formation of Au@

DOI: 10.1021/acs.chemmater.5b00199
Chem. Mater. 2015, 27, 2172–2180

Pd core−shell nanoparticles with no detectable Ag content according to the EDS results. Therefore, HCHO promoted the galvanic replacement reaction essentially by serving as a weak reducing agent to facilitate the reduction of Pd, which gave rise to increased cavity sizes and Pd:Ag ratios in comparison to those of nanostructures obtained with the same amounts of H_2PdCl_4 but in the absence of a reducing agent (Figure 2G). The structural and compositional evolution stopped upon the formation of the porous, double-walled nanoboxes (Figure 2H) because at this stage H_2PdCl_4 became incapable of further dealloying the Ag−Pd alloy walls even with the help of HCHO. The fully alloyed composition of the double-walled nanoboxes was further verified by the PXRD results as shown in Figure S10 of the Supporting Information.

In contrast to the mild reducing agents that promote the galvanic replacements, strong reducing agents may inhibit the galvanic replacement. It has been shown that in the presence of excessive strong reducing agents, exposing Ag nanoparticles to $AuCl_4^-$ resulted in conformally deposited Au thin layers on Ag nanoparticle surfaces while the galvanic replacement was effectively inhibited.[39,40] Here we found that $NaBH_4$, which was a strong reducing agent, completely inhibited the galvanic replacement between Ag nanocubes and H_2PdCl_4. As shown in Figure S12 of the Supporting Information, the Ag nanocubes maintained their structures and optical signatures well upon exposure to H_2PdCl_4 and $NaBH_4$, while small Pd nanoparticles (2−3 nm in diameter) formed in solution through vigorous reduction of Pd(II) by $NaBH_4$.

The shape of the sacrificial templates is another key factor determining the morphological evolution of nanoparticles upon galvanic replacement. The surface curvature of the Ag templates may affect the interfacial deposition, alloying, and dealloying processes and consequently introduce interesting modifications into the structures of the resulting hollow nanoparticles. Here we also investigated the galvanic replacement-induced structural evolution of single-crystalline Ag quasi-spherical nanoparticles in the absence and presence of reducing agents. The Ag quasi-spherical nanoparticles were obtained by etching the Ag nanocubes with $Fe(NO_3)_3$ following a previously reported method.[41] The preferential etching of Ag nanocube corners by $Fe(NO_3)_3$ resulted in the formation of truncated nanocubes, which further evolved into quasi-spherical nanoparticles eventually (see Figure S13 of the Supporting Information). While each single-crystalline Ag nanocube was enclosed by six well-defined, atomically flat {100} facets, the surfaces of the Ag quasi-spherical nanoparticles were locally curved. It was previously reported that the flat surfaces of nanocubes favored the conformal deposition of metallic layers and the subsequent alloying process during galvanic replacement, while increasing the surface curvature of the templates led to the deposition of discontinuous polycrystalline layers caused by larger interfacial distortion.[10,32] As a consequence, the as-obtained quasi-spherical nanoshells were composed of many nanocrystalline domains and their outer surfaces appeared to be much bumpier than those of the single-walled nanoboxes obtained using Ag nanocubes as the starting templates (see Figure S14 of the Supporting Information). In the absence of reducing agents, the hollowing of the quasi-spherical templates was hindered by the Pd nanocrystallites deposited on the outer surfaces of the Ag templates (Figure S14A,B of the Supporting Information). AA and HCHO effectively promoted both the inside-out hollowing processes and the Pd−Ag interdiffusion during alloying−dealloying processes upon galvanic replacements (Figure S14C−F of the Supporting Information). Interestingly, the AA-mediated galvanic replacement also led to the formation of multiple nanochambers enclosed by a quasi-spherical nanoshell (Figure S14C of the Supporting Information), which eventually evolved into single-cavity polycrystalline nanoshells as the amount of H_2PdCl_4 further increased (Figure S14D of the Supporting Information).

While the geometry-dependent plasmonic properties of Au and Ag nanostructures have been well-documented, the plasmonic tunability of Pd nanoparticles has been much less explored. Although significant progress has been made on the geometry-controlled synthesis of Pd nanostructures,[42] it remains much more challenging to fine-tune the plasmon resonances of Pd nanoparticles than to fine-tune their Au or Ag counterparts.[43−46] In addition to the limited tuning range of the plasmon resonances, the optical cross sections of pure Pd and Pd-containing multimetallic nanoparticles are much smaller than those of their Au or Ag counterparts because of strong plasmon damping. Figure 3A shows the extinction spectra of colloidal Ag−Pd bimetallic nanoparticles obtained upon galvanic replacement of Ag nanocubes with different amounts of H_2PdCl_4 in the absence of reducing agents. Because the extinction spectra were collected on colloidal samples with the same particle concentration (7×10^8 particles mL^{-1}), the

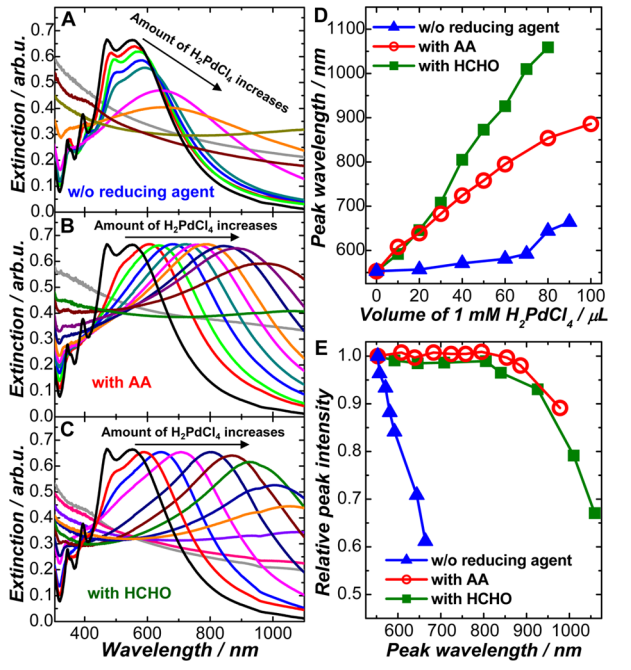

Figure 3. Extinction spectra of colloidal Ag−Pd bimetallic hollow nanostructures obtained through galvanic replacement of Ag nanocubes with various amounts of H_2PdCl_4 (A) in the absence of a reducing agent, (B) in the presence of AA, and (C) in the presence of HCHO. Panel A shows the extinction spectra of the samples obtained upon addition of 0, 20, 40, 60, 70, 80, 90, 100, 200, and 400 μL of 1 mM H_2PdCl_4. Panel B shows the extinction spectra of the samples obtained upon addition of 0, 10, 20, 30, 40, 50, 60, 80, 100, 150, 200, and 400 μL of 1 mM H_2PdCl_4. Panel C shows the extinction spectra of the samples obtained upon addition of 0, 10, 20, 30, 40, 50, 60, 70, 80, 100, 200, and 400 μL of 1 mM H_2PdCl_4. (D) Extinction peak wavelength as a function of the volume of the 1 mM H_2PdCl_4 solution. (E) Relative extinction peak intensity (normalized against the dipole plasmon resonance peak of Ag nanocubes) as a function of extinction peak wavelength.

DOI: 10.1021/acs.chemmater.5b00199
Chem. Mater. 2015, 27, 2172−2180

intensities of the measured optical extinction directly reflected the relative extinction cross sections of the nanoparticles. As the amount of H_2PdCl_4 increased, the dipole plasmon resonance progressively red-shifted while the extinction peak became significantly weaker and broader because of plasmon damping. The quadrupole and other higher-order multipole plasmon resonances were even more significantly damped than the dipole plasmon resonance upon galvanic replacement. When the volume of 1 mM H_2PdCl_4 was greater than 90 μL, the dipole plasmon peak completely disappeared in the visible and strong absorption feature emerged at wavelengths shorter than 550 nm due to the interband transitions in metallic Pd. The red-shift of the plasmon resonance can be interpreted as a consequence of the galvanic replacement-induced hollowing of the particles, while the plasmon damping is primarily caused by the incorporation of Pd into the nanoparticles.

Interestingly, the use of AA or HCHO allowed us to fine-tune, through galvanic replacement, the plasmon resonances of the Ag–Pd bimetallic nanostructures over much broader spectral ranges while the extinction peaks remained extremely robust across the visible into the near-infrared (see Figure 3B,C) in spite of the further enriched Pd content of the nanoparticles. The enhanced tunability of plasmon resonance frequencies was attributed to the larger cavity sizes and thinner wall thicknesses, while the enhanced robustness of the plasmon resonances may be due to the optimized Ag and Pd distributions in the hollow nanostructures. Without reducing agents, the interdiffusion between Ag and the deposited Pd may result in a compositional gradient in the alloy walls of the nanoparticles, which causes plasmon damping. This plasmon damping effect caused by surface deposition of Pd was also observed previously on Au@Pd core–shell nanoparticles[47−50] and was further confirmed in this work (Figures S9B and S11B of the Supporting Information). As discussed earlier in this paper, both AA and HCHO facilitated the alloying process during galvanic replacement, leading to the formation of more homogeneously mixed, fully alloyed Ag–Pd bimetallic walls. The effective diffusion of Pd into Ag matrix may allow the nanoparticles to inherit the strong plasmon resonances of Ag nanostructures without significant damping being caused by the Pd component. However, when the dealloying process began to dominate the structural evolution at high H_2PdCl_4 concentrations, significant plasmon damping was observed because of the loss of the Ag content in the nanoparticles (Figure 3B,C). The plasmon resonance peak completely disappeared when more than 200 μL of 1 mM H_2PdCl_4 was introduced. As summarized in Figure 3D, titrating Ag nanocubes with H_2PdCl_4 in the absence of reducing agents allowed us to tune only the plasmon resonances of Ag–Pd bimetallic nanoparticles in the wavelength range from ~550 to ~670 nm. With the aid of the mild reducing agents, the plasmonic tuning range was significantly expanded over the entire visible range and all the way to >1000 nm. As shown in Figure 3E, through AA- or HCHO-mediated galvanic replacements, the optical cross sections of the Ag–Pd bimetallic nanoparticles at the plasmon resonance wavelengths were well-maintained across the visible into the near-infrared whereas the optical cross sections of the nanoparticles dropped drastically upon galvanic replacement in the absence of reducing agents.

The enhanced capability of geometry control also allowed us to fine-tailor the interior and surface architectures of the Ag–Pd bimetallic nanostructures to optimize the catalytic competence of the particles. We used the catalytic hydrogenation of *p*-nitrophenol by $NaBH_4$ as a model reaction[51] to evaluate the catalytic activities of the Ag–Pd bimetallic nanostructures obtained through galvanic replacements under different conditions. UV–vis absorption spectroscopy was used to monitor the reaction kinetics in real time. When *p*-nitrophenol was mixed with $NaBH_4$, an absorption peak at ~400 nm was observed (Figure S15 of the Supporting Information), which was assigned to the absorption of *p*-nitrophenolate ions. Upon addition of the metallic nanoparticles, the intensity of the absorption peak at ~400 nm gradually decreased as the catalytic hydrogenation reaction proceeded. Meanwhile, an absorption band emerged at ~295 nm and became progressively more intense, indicating the formation of the product, *p*-aminophenol. We used the intensities of the absorption peak at 400 nm to quantify the reactant concentration as a function of reaction time. In Figure 4A–C, we directly compare the kinetics of the reactions catalyzed by the Ag nanocubes and various Ag–Pd bimetallic nanostructures at the same particle concentration of 2.0×10^8 particles mL^{-1}. In all these experiments, the initial concen-

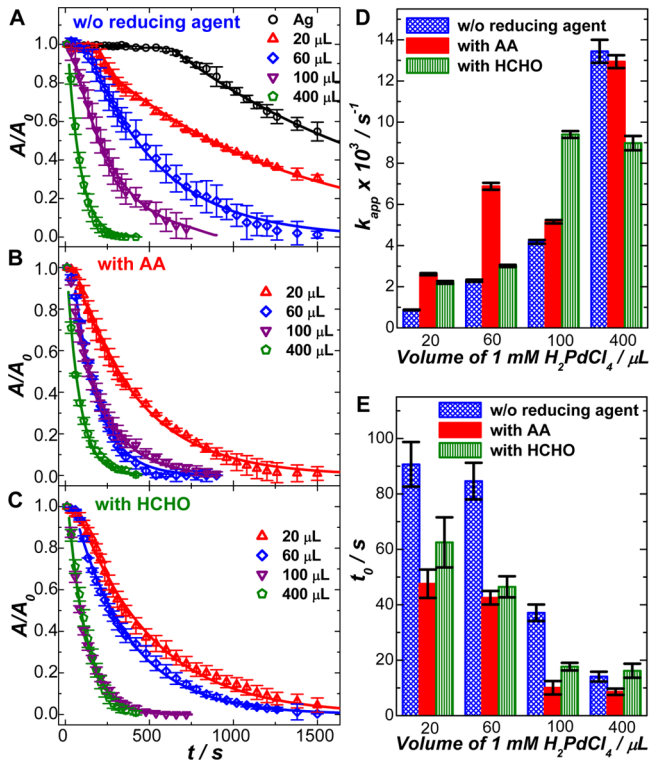

Figure 4. Absorption (normalized against the initial point) at 400 nm as a function of reaction time in the presence of Ag nanocubes and the Ag–Pd bimetallic hollow nanostructures obtained through galvanic replacement with various volumes of 1 mM H_2PdCl_4 as labeled in each panel (A) in the absence of reducing agents, (B) in the presence of AA, and (C) in the presence of HCHO. In all cases, the initial concentrations of *p*-nitrophenol and $NaBH_4$ were 43.2 μM and 8.64 mM, respectively. The concentration of Ag nanocubes and the Ag–Pd bimetallic hollow nanoparticles was 2.0×10^8 particles mL^{-1}. The error bars in panels A–C represent the standard deviations obtained from three experimental runs. The solid curves in panels A–C show the least-squares curve fitting results. (D) Apparent rate constants (k_{app}) and (E) induction times (t_0) of Ag–Pd bimetallic hollow nanostructures obtained through galvanic replacement under various conditions. The error bars in panels D and E represent the standard deviations obtained from least-squares curve fitting.

DOI: 10.1021/acs.chemmater.5b00199
Chem. Mater. 2015, 27, 2172–2180

trations of *p*-nitrophenol and $NaBH_4$ were 43.2 μM and 8.64 mM, respectively. While this reaction was extremely slow (no observable reaction over a few days) without nanoparticle catalysts, the metallic nanoparticles efficiently catalyzed the hydrogenation process. This metallic nanoparticle-catalyzed hydrogenation has been reported to be a multistep process.[51] Borohydride ions first adsorb on the surfaces of the metallic nanocatalysts to form an active hydrogen species, which subsequently hydrogenate the surface-adsorbed *p*-nitrophenol to form the product, *p*-aminophenol.

As shown in Figure 4A−C, after a certain period of induction time in which no reduction took place, the hydrogenation reaction followed a first-order rate law in the presence of excessive $NaBH_4$. The induction time may be ascribed to the time period required for the adsorption of *p*-nitrophenol and BH_4^- onto the nanoparticle surfaces.[52−54] An apparent rate constant was obtained through least-squares curve fitting using the following equation:

$$\frac{A}{A_0} = e^{-k_{app}(t-t_0)}$$

where A is the absorption intensity at 400 nm at particular time spots during the reaction, A_0 is absorption intensity at 400 nm before the reaction starts, t is the reaction time, t_0 is the induction time, and k_{app} is the apparent first-order rate constant. The kinetics measured by solution-phase UV−vis absorption spectroscopy reflects the overall reaction kinetics and thus strongly depends on the structures and surface properties of the nanocatalysts. For nanoparticles whose surfaces are capped with bulky organic ligands, the molecular diffusion may become much slower than the surface-catalyzed reaction step, making the overall kinetics diffusion-controlled.[55] Because the galvanic replacement reactions were conducted in the absence of any surface-capping ligands, the as-obtained Ag−Pd bimetallic nanoparticles had ligand-free surfaces that could be easily accessed by the reactant molecules. Therefore, the surface-catalyzed molecular transformation became the rate-limiting step, while the molecular diffusion associated with the adsorption/desorption steps was much faster.[51,56,57] As a consequence, pseudo-first-order reaction kinetics were observed here when $NaBH_4$ was in great excess.

In panels D and E of Figure 4, we compare the k_{app} and t_0 of the various Ag−Pd bimetallic nanostructures, respectively. An anticorrelated relationship between the apparent rate constants and the induction times was clearly observed. The Ag nanocubes had a significantly smaller k_{app} [$(6.9 \pm 1.6) \times 10^{-4}$ s^{-1}] and a longer t_0 (601 ± 11 s) in comparison to those of the Ag−Pd bimetallic nanostructures obtained through galvanic replacements. The enhanced catalytic activities of the Ag−Pd bimetallic nanostructures can be interpreted as a consequence of both the compositional and structural changes of the particles induced by the galvanic replacements. Pd may serve as a catalyst that is more active than Ag for hydrogenation reactions, and the Ag−Pd alloying that occurred during galvanic replacement may further improve the catalytic activities because of the synergy between Pd and Ag. A general trend was clearly observed that a higher Pd:Ag ratio gave rise to higher catalytic activities (larger k_{app} and shorter t_0). On the other hand, the galvanic replacement led to both interior hollowing and surface roughening of the nanoparticles, giving rise to significantly increased surface areas that can be exploited for catalysis. It is particularly interesting that the multichambered nanoboxes (60 μL of H_2PdCl_4 with AA) were catalytically more active than the single-walled nanoboxes (100 μL of H_2PdCl_4 with AA) in spite of their lower Pd content. The interior surfaces of the multichambered nanoboxes could also be accessed by the molecules because of the presence of pinholes in the outer walls and thus provided larger surface areas available for catalysis than the single-walled smooth nanoboxes. The surface roughening also allowed for the creation of highly curved local surface structures that served as highly active sites for catalysis. While the Ag nanocubes were enclosed predominantly by low-index {100} facets, the roughened surfaces of the Ag−Pd bimetallic hollow nanostructures were composed of a high fraction of coordinatively unsaturated surface atoms,[54,58−60] providing catalytically more active local high-index facets on the open surface structures of the particles. Considering all these compositional and geometric factors, the optimal catalytic activities observed on the Ag−Pd alloy hollow nanostructures with highly porous walls obtained upon addition of 400 μL of 1 mM H_2PdCl_4 can be interpreted as being the consequence of the synergistic effects of the enriched Pd content in the alloy walls, large surface areas, and the highly abundant under-coordinated surface atoms.

■ CONCLUSIONS

As shown in this work, a simple galvanic replacement reaction, when mediated by appropriate mild reducing agents, may provide a versatile pathway to fine-tailor the geometries of Ag−Pd bimetallic nanostructures, greatly enhancing our capabilities to fine-tune the optical and catalytic properties of these nanoparticles. Ag−Pd bimetallic nanostructures that are both optically tunable and catalytically active may find important applications in plasmon-driven photocatalysis,[61,62] molecular sensing,[63,64] and spectroscopic monitoring of catalytic reactions.[65,66] The optimization of the optical and catalytic properties of Ag−Pd bimetallic nanoparticles essentially relies on the capabilities to fine-control the particle geometries. The mild reducing agent-mediated galvanic replacement reported here not only allows us to fine-tailor the interior structures of the hollow nanoparticles to selectively fabricate single-chambered and multichambered nanoboxes but also provides a unique way to introduce nanoscale roughness and porosity to the nanobox walls. The Ag−Pd bimetallic hollow nanostructures obtained through this reducing agent-mediated galvanic replacement exhibit greatly enhanced plasmonic tunability over a much broader spectral range with minimized plasmon damping in comparison to that of the nanoparticles obtained through reducing agent-free galvanic replacement. The enhanced geometric controllability further allows us to achieve optimized catalytic activities toward the room-temperature hydrogenation of *p*-nitrophenol by judiciously tailoring the compositions, interior structures, and surface architectures of the Ag−Pd bimetallic nanoparticles.

■ EXPERIMENTAL SECTION

Chemicals and Materials. All chemicals were obtained from commercial suppliers and used without further purification. Ethylene glycol (EG), anhydrous potassium carbonate (K_2CO_3, granular), and formaldehyde (37 wt % solution) were purchased from J. T. Baker. Polyvinylpyrrolidone [PVP, average molecular weight (MW) of 58000], hydrogen tetrachloroaurate trihydrate ($HAuCl_4 \cdot 3H_2O$, ACS, 99.99% metals basis), silver nitrate ($AgNO_3$, 99.9995% metals basis), and iron(III) nitrate [$Fe(NO_3)_3 \cdot 9H_2O$, >98% metals basis] were purchased from Alfa Aesar. L-Ascorbic acid (BioUltra, ≥99.5%), sodium borohydride ($NaBH_4$, 99%), hydrochloric acid (HCl, 37 wt % in water), silver trifluoroacetate (CF_3COOAg, ≥99.99% trace metals

DOI: 10.1021/acs.chemmater.5b00199
Chem. Mater. 2015, 27, 2172−2180

basis), sodium hydrosulfide hydrate ($NaHS{\cdot}xH_2O$), and palladium(II) chloride ($PdCl_2$, ≥99.9%) were purchased from Sigma-Aldrich. Ultrapure water (18.2 MΩ resistivity, Barnstead EasyPure II 7138) was used for all experiments. All glassware was cleaned using freshly prepared aqua regia (3:1 HCl:HNO_3 ratio by volume) followed by a thorough rinse with a copious amount of water.

Galvanic Replacements of Ag Nanocubes with H_2PdCl_4. Monodisperse Ag nanocubes with an average edge length of 100 nm were fabricated following the protocol developed by Xia and co-workers[67] with slight modifications. More experimental details of Ag nanocube fabrication are presented in the Supporting Information.

In a typical galvanic replacement reaction, 30 μL of an aqueous suspension of Ag nanocubes (5×10^{10} particles mL^{-1}) was added to 2 mL of ultrapure water in a small glass vial while being magnetically stirred. Then 50 μL of 50 mM freshly prepared AA, 100 μL of 37 wt % HCHO, or 50 μL of 50 mM freshly prepared $NaBH_4$ and various volumes (10−400 μL) of a 1 mM H_2PdCl_4 aqueous solution were introduced into the system in sequence at room temperature. A 10 mM H_2PdCl_4 aqueous solution was prepared by dissolving 0.001 mol of $PdCl_2$ in 100 mL of 0.02 M HCl at an elevated temperature of 60 °C while being magnetically stirred and then diluted to a concentration of 1 mM. Galvanic replacement reactions were also conducted with exactly the same amounts of Ag nanocubes and H_2PdCl_4 but in the absence of any reducing agent. All the galvanic replacement reactions were conducted at room temperature for 1 h. Under the current experimental conditions, the galvanic replacement reactions were observed to be kinetically fast and the reactions were completed over time periods ranging from a few seconds to a few minutes. The Ag−Pd bimetallic nanoparticles were centrifuged (4.0 rpm, 4 min), washed with water twice, and finally redispersed in 50 μL of water. The particle concentration of the as-obtained Ag−Pd bimetallic nanoparticles was 3×10^{10} particles mL^{-1}.

We also studied the galvanic replacement between Ag quasi-spherical nanoparticles and H_2PdCl_4 under the same experimental conditions. The Ag quasi-spherical nanoparticles were fabricated through etching of Ag nanocubes with $Fe(NO_3)_3$ following a previously published protocol.[41] More experimental details about the fabrication of truncated Ag nanocubes and Ag quasi-spherical nanoparticles were included in the Supporting Information.

Au Nanoparticle-Seeded Ag and Pd Deposition. Au nanoparticles with average radius of ∼47 nm were synthesized by reducing chloroauric acid with formaldehyde at room temperature.[68] More experimental details about the fabrication of Au nanoparticles can be found in the Supporting Information. The core−shell nanoparticles were synthesized through Au nanoparticle-seeded electroless plating of Ag, Pd, or Ag−Pd alloy at room temperature. Briefly, 0.1 mL of a Au colloidal solution (6×10^{10} particles mL^{-1}) was added into 2 mL of ultrapure H_2O. Then 50 μL of 50 mM AA or 100 μL of 37 wt % HCHO was added to the solution followed by the introduction of 30 μL of 0.01 M $AgNO_3$, 100 μL of 1 mM H_2PdCl_4, or a mixture of 30 μL of 0.01 M $AgNO_3$ and 100 μL of 1 mM H_2PdCl_4 while being magnetically stirred. The reactant mixtures were stirred for 30 min, and the resulting nanoparticles were centrifuged (1500 rcf, 5 min), washed twice with water, and finally redispersed in water (final concentration of $\sim 1.2 \times 10^9$ particles mL^{-1}).

Characterization. The morphologies and structures of the nanoparticles were characterized by TEM using a Hitachi H-8000 transmission electron microscope, which was operated at an accelerating voltage of 200 kV. HRTEM images were obtained using a JEOL 2100F 200 kV FEG-STEM/TEM microscope. All samples for TEM measurements were dispersed in water and drop-dried on 400 mesh carbon-coated Cu grids (Electron Microscopy Science Inc.). The structures and compositions of the nanoparticles were also characterized by SEM and EDS measurements using a Zeiss Ultraplus thermal field emission scanning electron microscope. The samples for SEM and EDS measurements were dispersed in water and drop-dried on silicon wafers. PXRD patterns were recorded using a Rigaku D/Max 2100 powder X-ray diffractometer with a Cu Kα radiation source (λ = 1.544 Å). The optical extinction spectra of the nanoparticles were measured on aqueous colloidal suspensions at room temperature, using a Beckman Coulter Du 640 spectrophotometer.

Nanoparticle-Catalyzed Hydrogenation of *p*-Nitrophenol. The hydrogenation of *p*-nitrophenol by $NaBH_4$ was used as a model reaction to evaluate the catalytic performances of Ag−Pd bimetallic nanoparticles. In a typical procedure, 100 μL of 1.0 mM *p*-nitrophenol and 200 μL of 0.1 M $NaBH_4$ (freshly prepared, ice-cold) were sequentially added to 2.0 mL of ultrapure water in a quartz cuvette and mixed thoroughly. Fifteen microliters of colloidal Ag−Pd bimetallic nanoparticles was then introduced into the mixture to yield a final concentration of 2×10^8 particles mL^{-1}. After the sample had been thoroughly mixed for 5 s, UV−vis extinction spectra were recorded in real time to monitor the catalytic reaction process using a Beckman Coulter Du 640 spectrophotometer at room temperature.

■ ASSOCIATED CONTENT

Ⓢ Supporting Information

Additional experimental details, SEM images, TEM images, EDS results, HRTEM images, PXRD patterns, and UV−vis extinction spectra as noted in the text. This material is available free of charge via the Internet at http://pubs.acs.org.

■ AUTHOR INFORMATION

Corresponding Author

*E-mail: wang344@mailbox.sc.edu. Phone: (803) 777-2203. Fax: (803) 777-9521.

Notes

The authors declare no competing financial interest.

■ ACKNOWLEDGMENTS

This work was supported by the University of South Carolina Office of Vice President for Research through an ASPIRE-I Track-I Award. We thank Dr. Douglas A. Blom of the University of South Carolina Nanocenter for HRTEM measurements and the University of South Carolina Electron Microscopy Center for instrument use and technical assistance.

■ REFERENCES

(1) Sun, Y. G.; Xia, Y. N. *Science* **2002**, *298*, 2176−2179.
(2) Cobley, C. M.; Xia, Y. N. *Mater. Sci. Eng., R* **2010**, *70*, 44−62.
(3) Xia, X. H.; Wang, Y.; Ruditskiy, A.; Xia, Y. N. *Adv. Mater. (Weinheim, Ger.)* **2013**, *25*, 6313−6333.
(4) Gonzalez, E.; Arbiol, J.; Puntes, V. F. *Science* **2011**, *334*, 1377−1380.
(5) Sun, Y. G.; Xia, Y. N. *Anal. Chem.* **2002**, *74*, 5297−5305.
(6) Skrabalak, S. E.; Au, L.; Li, X. D.; Xia, Y. N. *Nat. Protoc.* **2007**, *2*, 2182−2190.
(7) Skrabalak, S. E.; Chen, J. Y.; Sun, Y. G.; Lu, X. M.; Au, L.; Cobley, C. M.; Xia, Y. N. *Acc. Chem. Res.* **2008**, *41*, 1587−1595.
(8) Metraux, G. S.; Cao, Y. C.; Jin, R. C.; Mirkin, C. A. *Nano Lett.* **2003**, *3*, 519−522.
(9) Sun, Y. G.; Xia, Y. N. *Nano Lett.* **2003**, *3*, 1569−1572.
(10) Sun, Y. G.; Xia, Y. N. *J. Am. Chem. Soc.* **2004**, *126*, 3892−3901.
(11) Sun, Y. G.; Wiley, B.; Li, Z. Y.; Xia, Y. N. *J. Am. Chem. Soc.* **2004**, *126*, 9399−9406.
(12) Khalavka, Y.; Becker, J.; Sonnichsen, C. *J. Am. Chem. Soc.* **2009**, *131*, 1871−1875.
(13) Cho, E. C.; Camargo, P. H. C.; Xia, Y. N. *Adv. Mater. (Weinheim, Ger.)* **2010**, *22*, 744−748.
(14) Xiong, W.; Sikdar, D.; Walsh, M.; Si, K. J.; Tang, Y.; Chen, Y.; Mazid, R.; Weyland, M.; Rukhlenko, I. D.; Etheridge, J.; Premaratne, M.; Li, X. Y.; Cheng, W. L. *Chem. Commun.* **2013**, *49*, 9630−9632.
(15) Yang, Y.; Zhang, Q.; Fu, Z. W.; Qin, D. *ACS Appl. Mater. Interfaces* **2014**, *6*, 3750−3757.

DOI: 10.1021/acs.chemmater.5b00199
Chem. Mater. 2015, 27, 2172−2180

(16) McEachran, M.; Keogh, D.; Pietrobon, B.; Cathcart, N.; Gourevich, I.; Coombs, N.; Kitaev, V. *J. Am. Chem. Soc.* **2011**, *133*, 8066−8069.
(17) Hong, X.; Wang, D. S.; Cai, S. F.; Rong, H. P.; Li, Y. D. *J. Am. Chem. Soc.* **2012**, *134*, 18165−18168.
(18) Chen, J.; Saeki, F.; Wiley, B. J.; Cang, H.; Cobb, M. J.; Li, Z. Y.; Au, L.; Zhang, H.; Kimmey, M. B.; Li, X. D.; Xia, Y. N. *Nano Lett.* **2005**, *5*, 473−477.
(19) Chen, J. Y.; Wiley, B.; Li, Z. Y.; Campbell, D.; Saeki, F.; Cang, H.; Au, L.; Lee, J.; Li, X. D.; Xia, Y. N. *Adv. Mater. (Weinheim, Ger.)* **2005**, *17*, 2255−2261.
(20) Xia, Y. N.; Li, W. Y.; Cobley, C. M.; Chen, J. Y.; Xia, X. H.; Zhang, Q.; Yang, M. X.; Cho, E. C.; Brown, P. K. *Acc. Chem. Res.* **2011**, *44*, 914−924.
(21) Yavuz, M. S.; Cheng, Y. Y.; Chen, J. Y.; Cobley, C. M.; Zhang, Q.; Rycenga, M.; Xie, J. W.; Kim, C.; Song, K. H.; Schwartz, A. G.; Wang, L. H. V.; Xia, Y. N. *Nat. Mater.* **2009**, *8*, 935−939.
(22) Chen, J. Y.; Wiley, B.; McLellan, J.; Xiong, Y. J.; Li, Z. Y.; Xia, Y. N. *Nano Lett.* **2005**, *5*, 2058−2062.
(23) Mahmoud, M. A.; El-Sayed, M. A. *Langmuir* **2012**, *28*, 4051−4059.
(24) Popa, A.; Samia, A. C. S. *Chem. Commun.* **2014**, *50*, 7295−7298.
(25) Zheng, T. T.; Zhang, Q. F.; Feng, S.; Zhu, J. J.; Wang, Q.; Wang, H. *J. Am. Chem. Soc.* **2014**, *136*, 2288−2291.
(26) Tsuji, M.; Kidera, T.; Yajima, A.; Hamasaki, M.; Hattori, M.; Tsuji, T.; Kawazumi, H. *CrystEngComm* **2014**, *16*, 2684−2691.
(27) Zhang, W. Q.; Yang, J. Z.; Lu, X. M. *ACS Nano* **2012**, *6*, 7397−7405.
(28) Chen, C.; Kang, Y. J.; Huo, Z. Y.; Zhu, Z. W.; Huang, W. Y.; Xin, H. L. L.; Snyder, J. D.; Li, D. G.; Herron, J. A.; Mavrikakis, M.; Chi, M. F.; More, K. L.; Li, Y. D.; Markovic, N. M.; Somorjai, G. A.; Yang, P. D.; Stamenkovic, V. R. *Science* **2014**, *343*, 1339−1343.
(29) Mahmoud, M. A.; Saira, F.; El-Sayed, M. A. *Nano Lett.* **2010**, *10*, 3764−3769.
(30) Zhang, H.; Jin, M. S.; Liu, H. Y.; Wang, J. G.; Kim, M. J.; Yang, D. R.; Xie, Z. X.; Liu, J. Y.; Xia, Y. N. *ACS Nano* **2011**, *5*, 8212−8222.
(31) Mahmoud, M. A.; Garlyyev, B.; El-Sayed, M. A. *J. Phys. Chem. Lett.* **2014**, *5*, 4088−4094.
(32) Gilroy, K. D.; Farzinpour, P.; Sundar, A.; Hughes, R. A.; Neretina, S. *Chem. Mater.* **2014**, *26*, 3340−3347.
(33) Sutter, E.; Jungjohann, K.; Bliznakov, S.; Courty, A.; Maisonhaute, E.; Tenney, S.; Sutter, P. *Nat. Commun.* **2014**, *5*, 5946 DOI: 10.1038/ncomms5946.
(34) Cobley, C. M.; Campbell, D. J.; Xia, Y. N. *Adv. Mater. (Weinheim, Ger.)* **2008**, *20*, 748−752.
(35) Mech, K.; Zabinski, P.; Kowalik, R.; Fitzner, K. *J. Electrochem. Soc.* **2013**, *160*, H770−H774.
(36) Jing, H.; Large, N.; Zhang, Q. F.; Wang, H. *J. Phys. Chem. C* **2014**, *118*, 19948−19963.
(37) Zhou, F.; Li, Z. Y.; Liu, Y.; Xia, Y. N. *J. Phys. Chem. C* **2008**, *112*, 20233−20240.
(38) Yin, Y. D.; Rioux, R. M.; Erdonmez, C. K.; Hughes, S.; Somorjai, G. A.; Alivisatos, A. P. *Science* **2004**, *304*, 711−714.
(39) Yang, Y.; Liu, J. Y.; Fu, Z. W.; Qin, D. *J. Am. Chem. Soc.* **2014**, *136*, 8153−8156.
(40) Shahjamali, M. M.; Bosman, M.; Cao, S. W.; Huang, X.; Saadat, S.; Martinsson, E.; Aili, D.; Tay, Y. Y.; Liedberg, B.; Loo, S. C. J.; Zhang, H.; Boey, F.; Xue, C. *Adv. Funct. Mater.* **2012**, *22*, 849−854.
(41) Cobley, C. M.; Rycenga, M.; Zhou, F.; Li, Z. Y.; Xia, Y. N. *J. Phys. Chem. C* **2009**, *113*, 16975−16982.
(42) Xiong, Y. J.; Xia, Y. N. *Adv. Mater. (Weinheim, Ger.)* **2007**, *19*, 3385−3391.
(43) Xiong, Y. J.; McLellan, J. M.; Chen, J. Y.; Yin, Y. D.; Li, Z. Y.; Xia, Y. N. *J. Am. Chem. Soc.* **2005**, *127*, 17118−17127.
(44) Huang, X. Q.; Tang, S. H.; Mu, X. L.; Dai, Y.; Chen, G. X.; Zhou, Z. Y.; Ruan, F. X.; Yang, Z. L.; Zheng, N. F. *Nat. Nanotechnol.* **2011**, *6*, 28−32.
(45) Niu, W. X.; Zhang, W. Q.; Firdoz, S.; Lu, X. M. *Chem. Mater.* **2014**, *26*, 2180−2186.
(46) Niu, Z. Q.; Zhen, Y. R.; Gong, M.; Peng, Q.; Nordlander, P.; Li, Y. D. *Chem. Sci.* **2011**, *2*, 2392−2395.
(47) Chen, H. J.; Wang, F.; Li, K.; Woo, K. C.; Wang, J. F.; Li, Q.; Sun, L. D.; Zhang, X. X.; Lin, H. Q.; Yan, C. H. *ACS Nano* **2012**, *6*, 7162−7171.
(48) Jing, H.; Wang, H. *CrystEngComm* **2014**, *16*, 9469−9477.
(49) Wang, F.; Sun, L. D.; Feng, W.; Chen, H. J.; Yeung, M. H.; Wang, J. F.; Yan, C. H. *Small* **2010**, *6*, 2566−2575.
(50) Xiang, Y. J.; Wu, X. C.; Liu, D. F.; Jiang, X. Y.; Chu, W. G.; Li, Z. Y.; Ma, Y.; Zhou, W. Y.; Xie, S. S. *Nano Lett.* **2006**, *6*, 2290−2294.
(51) Herves, P.; Perez-Lorenzo, M.; Liz-Marzan, L. M.; Dzubiella, J.; Lu, Y.; Ballauff, M. *Chem. Soc. Rev.* **2012**, *41*, 5577−5587.
(52) Sarkar, S.; Sinha, A. K.; Pradhan, M.; Basu, M.; Negishi, Y.; Pal, T. *J. Phys. Chem. C* **2011**, *115*, 1659−1673.
(53) Zeng, J.; Zhang, Q.; Chen, J. Y.; Xia, Y. N. *Nano Lett.* **2010**, *10*, 30−35.
(54) Zhang, Q. F.; Blom, D. A.; Wang, H. *Chem. Mater.* **2014**, *26*, 5131−5142.
(55) Esumi, K.; Isono, R.; Yoshimura, T. *Langmuir* **2004**, *20*, 237−243.
(56) Wunder, S.; Polzer, F.; Lu, Y.; Mei, Y.; Ballauff, M. *J. Phys. Chem. C* **2010**, *114*, 8814−8820.
(57) Wunder, S.; Lu, Y.; Albrecht, M.; Ballauff, M. *ACS Catal.* **2011**, *1*, 908−916.
(58) Tian, N.; Zhou, Z. Y.; Sun, S. G.; Ding, Y.; Wang, Z. L. *Science* **2007**, *316*, 732−735.
(59) Quan, Z. W.; Wang, Y. X.; Fang, J. Y. *Acc. Chem. Res.* **2013**, *46*, 191−202.
(60) Zhang, H.; Jin, M. S.; Xia, Y. N. *Angew. Chem., Int. Ed.* **2012**, *51*, 7656−7673.
(61) Wang, F.; Li, C. H.; Chen, H. J.; Jiang, R. B.; Sun, L. D.; Li, Q.; Wang, J. F.; Yu, J. C.; Yan, C. H. *J. Am. Chem. Soc.* **2013**, *135*, 5588−5601.
(62) Kale, M. J.; Avanesian, T.; Christopher, P. *ACS Catal.* **2014**, *4*, 116−128.
(63) Langhammer, C.; Zoric, I.; Kasemo, B. *Nano Lett.* **2007**, *7*, 3122−3127.
(64) Tang, M. L.; Liu, N.; Dionne, J. A.; Alivisatos, A. P. *J. Am. Chem. Soc.* **2011**, *133*, 13220−13223.
(65) Jing, H.; Zhang, Q. F.; Large, N.; Yu, C. M.; Blom, D. A.; Nordlander, P.; Wang, H. *Nano Lett.* **2014**, *14*, 3674−3682.
(66) Huang, J. F.; Zhu, Y. H.; Lin, M.; Wang, Q. X.; Zhao, L.; Yang, Y.; Yao, K. X.; Han, Y. *J. Am. Chem. Soc.* **2013**, *135*, 8552−8561.
(67) Xia, X. H.; Zeng, J.; Oetjen, L. K.; Li, Q. G.; Xia, Y. N. *J. Am. Chem. Soc.* **2012**, *134*, 1793−1801.
(68) Zhang, L.; Blom, D. A.; Wang, H. *Chem. Mater.* **2011**, *23*, 4587−4598.

DOI: 10.1021/acs.chemmater.5b00199
Chem. Mater. 2015, 27, 2172−2180